Photoacoustics 3 (2015) 151–158

Contents lists available at ScienceDirect

Photoacoustics

journal homepage: www.elsevier.com/locate/pacs

Optoacoustic image segmentation based on signal domain analysis

Christian Lutzweiler [a,b], Reinhard Meier [c,d], Daniel Razansky [a,c,*]

[a] Institute for Biological and Medical Imaging (IBMI), Helmholtz Center Munich, Neuherberg, Germany
[b] School of Electrical and Computer Engineering, Technische Universität München, Munich, Germany
[c] School of Medicine, Technische Universität München, Munich, Germany
[d] Department of Diagnostic and Interventional Radiology, University Hospital of Ulm, Ulm, Germany

ARTICLE INFO

Article history:
Received 9 November 2015
Accepted 18 November 2015
Available online 30 November 2015

Keywords:
Optoacoustics
Photoacoustic Tomography
Clinical Imaging
Acoustic Properties
Reconstruction
Image Segmentation

ABSTRACT

Efficient segmentation of optoacoustic images has importance in enhancing the diagnostic and quantification capacity of this modality. It may also aid in improving the tomographic reconstruction accuracy by accounting for heterogeneous optical and acoustic tissue properties. In particular, when imaging through complex biological tissues, the real acoustic properties often deviate considerably from the idealized assumptions of homogenous conditions, which may lead to significant image artifacts if not properly accounted for. Although several methods have been proposed aiming at estimating and accounting for the complex acoustic properties in the image domain, accurate delineation of structures is often hindered by low contrast of the images and other artifacts produced due to incomplete tomographic coverage and heuristic assignment of the tissue properties during the reconstruction process. In this letter, we propose instead a signal domain analysis approach that retrieves acoustic properties of the object to be reconstructed from characteristic features of the detected optoacoustic signals prior to image reconstruction. Performance of the proposed method is first tested in simulation and experiment using two-dimensional tissue-mimicking phantoms. Significant improvements in the segmentation abilities and overall reconstructed image quality are further showcased in experimental cross-sectional data acquired from a human finger.

1. Text

Owing to the hybrid nature of optoacoustics, generation and detection of signals is affected by both the optical and acoustic properties of the imaged object as well as of the imaging system employed [1,2]. Thermal energy resulting from absorption of the excitation pulsed light is converted into propagating acoustic pressure waves, which are subsequently recorded by a set of detectors surrounding the object [3,4]. In the first image reconstruction step, the distribution of the deposited optical energy is restored from the measured time-resolved signals by assuming a specific acoustic propagation model [4]. The ability to quantitatively interpret the reconstructed images implies a second step based on a light propagation model, which is aimed at reconstructing the map of the optical absorption coefficient from the restored thermal energy distribution [2]. Idealized ultrasound propagation, namely a uniform medium with constant speed-of-sound (SoS) and free of acoustic absorption and scattering, is commonly assumed in order to perform the first reconstruction step [4]. However, acoustic properties of real biological tissues may deviate from the idealized assumptions, e.g., the SoS may significantly vary even among different soft tissues, from 1450 m/s in fat to 1600 m/s in muscle tissue, as compared to 1500 m/s in water at room temperature [5]. The use of average (homogenous) acoustic parameters for optoacoustic reconstructions may consequently result in image blurring, loss of features and deterioration of the overall imaging quality [6].

For accurate optoacoustic image reconstruction, the inverse method therefore needs to be capable of taking into account the heterogeneous distribution of the acoustic properties in the imaged object. Analytic reconstruction methods, such as back-projection or series expansion, are mostly based on the assumption of a uniform acoustic medium, making them not suitable for this purpose. In contrast, numerical methods are usually employed to efficiently account for the non-uniform acoustic properties. For instance, the model-based (MB) class of inverse algorithms has been shown capable of modeling the effects of heterogeneous SoS or absorption [6,7]. Even more flexible than MB approaches are time reversal (or more general finite-time differences) algorithms, which are based on repeated application of a time-propagation operator directly obtained from the discretized wave equation [8,9]. In this way, heterogeneous maps of SoS, impedance mismatches, or acoustic attenuation are

* Corresponding author.
E-mail address: dr@tum.de (D. Razansky).

http://dx.doi.org/10.1016/j.pacs.2015.11.002

seamlessly included during the reconstruction with effects like correct time-of-flight (TOF), ultrasonic refraction, or reflection readily accounted for as well.

Nonetheless, provided a suitable reconstruction approach has been identified, the acoustic reconstruction parameters still need to be determined. In most cases, the exact distribution of the acoustic properties in the medium is not known. Thus they need to be assigned heuristically, optimized numerically in combination with the absorption distribution, or determined experimentally. The latter can be done using additional transmit-receive or passive ultrasound scans of the object [10]. If ultrasound data is not available, optoacoustic image segmentation offers an alternative way to discern regions with different physical properties from e.g. boundary detection or texture analysis followed by an autofocusing step to assign the optimal parameters to those regions [11]. However, automated segmentation in the image domain is often complicated by the low contrast of the images, other artifacts, and blurring resulting from reconstruction imperfections, such as an incomplete tomographic coverage or heuristic (inaccurate) assignment of tissue properties during the reconstruction process.

In this letter, we instead harvested characteristic features of the measured data in the signal domain in order to perform segmentation and to obtain acoustic parameters for optimized optoacoustic reconstructions. In many experimental scenarios, absorption and acoustic properties of the imaged objects exhibit a few dominant features that can be linked in a simplified manner to allow for effective optoacoustic signal domain analysis and parameter retrieval.

Tomographic optoacoustic data consists of many individual projections, i.e. time-domain signals taken at several time instants at one given detector angle. The ensemble of the projections for all detection locations (e.g. regularly distributed on a circle for typical 2-D tomographic systems) is called a sinogram, denoted here by $S(t,\varphi)$. Image pixels that contribute to the optoacoustic signal value recorded at a given projection φ and time instant t are distributed on a circle of radius $d = c{\cdot}t$ (c denotes the SoS) with its center located at the detector position (Fig. 1(a), black dashed arcs). If tomographic data is complete (i.e. the detection circle fully surrounds the object), the individual optoacoustic signals will have redundancy with respect to all time points before and after the time point corresponding to the center of the tomographic scanning geometry [12]. A similar 'redundancy' of the sinogram occurs for opposite detectors: If a strongly absorbing boundary (black cross) orthogonal to the direct path (1) to the detector (black arrow and dashed arc) creates a large signal at the corresponding detector at time instant t_1, the opposite detector (2) would sense a highly correlated or even redundant signal at t_2 (Fig. 1(a) and 1(b)). This redundancy in the projection data can be exploited to obtain the acoustic properties of the medium, e.g. to determine the average SoS in the medium by considering t_1, t_2, and the radius of the detection surface. Likewise, by detecting both directly propagating (1′) and reflected (3) signals (white cross) from an acoustically reflecting boundary (white circle), one may determine its location in space.

In order to perform segmentation and to extract optimized reconstruction parameters directly from the individual projection data, our proposed signal domain analysis is based on common assumptions fulfilled for many realistic cross-sectional optoacoustic imaging scenarios, e.g. when imaging small animals or human fingers [13,14]:

- The imaged volume can be effectively divided into two main compartments having different yet constant acoustic properties. It is then anticipated that the optimized reconstruction approach considering the different properties would yield better quality images as compared to the best reconstruction achievable under assumptions of homogeneous (average) acoustic properties in the entire medium.
- The boundary $R\left(\varphi_{img}\right)$ between the two compartments is convex and smooth–as is the case for cross-sectional imaging of e.g. small animals and human fingers. The boundary radius $R\left(\varphi_{img}\right)$ is described by a small set of suitable parameters, e.g. the first few harmonics.
- The outer compartment, usually consisting of a coupling medium (e.g. water, gel, or a solid acoustic couplant), only has insignificant optical absorption as compared to the inner compartment. The acoustic parameters of the former are assumed to be known for the given ambient temperature. On the other hand, the shape of the compartment does not have to be known a priori.
- The inner compartment is typically associated with the object to be imaged, which is assumed to have low internal variations in its acoustic properties as compared to the global difference with respect to the outer compartment, e.g. various tissues versus water. In addition, significant light absorption and attenuation takes place close to the boundary between the two compartments, a realistic assumption for most biological objects.
- Nonetheless, a third compartment with a strong acoustic impedance mismatch can be added. Its dominant effect is inducing internal reflections of the optoacoustic signals originating from within the inner compartment. Such strong mismatches may occur e.g. at the boundaries of bones or at air cavities.
- To avoid significant limited-view artifacts, the detection surface should have a large angular coverage around the imaged object, ideally more than 180°.

In short, the proposed method can be described as follows: The signals are transformed into a Hilbert domain to facilitate analysis while retaining the key signal features. Examples of such features can be seen in signals like (1), (2), and (3) in Fig. 1(b), all originating from absorption at the boundary. Variations in both spatial distribution of the absorbers or acoustic propagation properties may result in optoacoustic signal alterations. For instance, a larger phantom size would result in an earlier detection of the first signals (1) while a smaller SoS within the phantom would lead to a delayed arrival of the signal features (2) and (3). A simplistic, low dimensional model can predict the corresponding time of arrival given the known phantom shape or the SoS. In turn, one may consider solving the inverse problem of obtaining the unknown acoustic parameters from the extracted signal features. Such a methodology is of high computational efficiency because the iterative optimization is performed by only considering one (or a few) unknowns without involving calculations with thousands of pixels or multiple time consuming image reconstruction procedures.

In detail, the proposed method is based on the following steps and assumptions: As can be noticed from Fig. 1(a) and 1(b), distinct image features would result in similarly distinct sinogram features. For the purpose of feature extraction in the signal domain, the absolute value of the Hilbert-transformed (with respect to time) sinogram is taken, denoted here by $H(t,\varphi)$. In this way, the measured bipolar signals are transformed into unipolar signals that are more suitable for feature extraction by maximization. In order to perform signal domain analysis and finally render the desired model parameters, a parameterized, time-of-flight-based model function $TOF(\varphi,\boldsymbol{m})$ is subsequently used. $TOF(\varphi,\boldsymbol{m})$ calculates the signal TOF for given source locations and acoustic properties as a function of detector position φ (considering the minimal TOF according to Fermat's principle). In the examples below, the sought-after set of parameters of the model, $\mathbf{m}$, consists of the SoS within the imaged object, of the parameterized boundary between the compartments or of the reflecting interface. Thus, $TOF(\varphi,\boldsymbol{m})$ is a simplistic, low dimensional acoustic propagation model that relates parameterized signal origin, propagation according to parameterized acoustic properties, and time of arrival at the detection location. The three

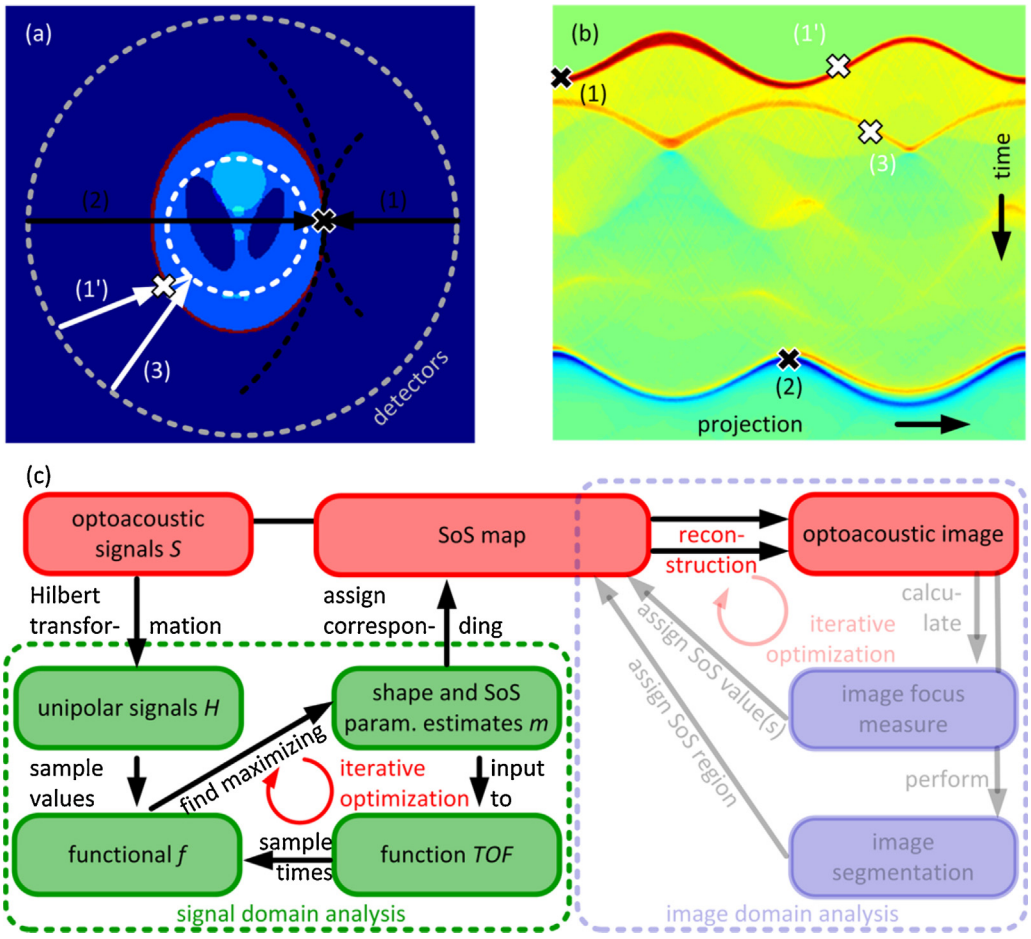

Fig. 1. Concept of signal domain analysis. (a) At the absorbing boundary (black cross) of the numerical phantom huge signals will be detected at detector locations ((1) and (2)) with a tangential integration arc (dashed black line). Opposite detectors provide partially redundant information and consequently information on the SoS. Accordingly, boundary signals (white cross) with direct (1′) and indirect (3) propagation provide information on the location of a reflecting boundary (white dashed line). (b) Corresponding sinogram with signal features corresponding to those in the image domain in (a). (c) Workflow of the proposed algorithm: Instead of performing reconstructions (red) with a heuristically assumed SoS map, signal domain analysis (green) is performed prior to reconstruction. Unipolar signals H are generated from the measured bipolar signals S by applying a Hilbert transformation with respect to the time variable. The optimized SoS parameters are obtained by retrieving characteristic features in the signals via maximizing the low dimensional functional f depending on acoustic parameters m through TOF and on the signals H. Subsequently, only a single reconstruction process with an optimized SoS map has to be performed. Conversely, for image domain methods (pale blue) the computationally expensive reconstruction procedure has to be performed multiple times as part of the optimization process.

TOF-functions use a model for: 1. The shortest (direct) propagation time as a function of the detection angle and compartment boundary parameters ($TOF1(\varphi, \boldsymbol{m})$), i.e. it allows for determining the shape of the compartments; 2. The longest (transmission) propagation time for the boundary signals as a function of detection angle and SoS within the object ($TOF2(\varphi, \boldsymbol{m})$), i.e. it allows for determining the SoS of the inner compartment; 3. The reflected signal propagation time as a function of the detection angle and reflector boundary ($TOF3(\varphi, \boldsymbol{m})$), i.e. it allows for determining the shape of the reflecting boundary. The corresponding processes and signals are labeled by (1), (2), and (3) in Fig. 1(a) and (b), respectively.

Model parameters are consequently obtained by numerical maximization of a functional f with respect to $\mathbf{m}$. f is the sum of the Hilbert-transformed sinogram H for all projections, each corresponding to one specific time instant as predicted by $TOF(\varphi, \boldsymbol{m})$. For a suitable selection of model parameters $\mathbf{m}$, shape of the signal feature predicted by $TOF(\varphi, \boldsymbol{m})$ is highly correlated with the signals, thus a maximum value of the functional f is expected. Conversely, for an arbitrary choice of $\mathbf{m}$ no pronounced correlation is expected, thus the functional is not maximized. Optimized acoustic parameters $\mathbf{m}$ are then obtained via

$$\boldsymbol{m} = \mathrm{argmax}_m f(\boldsymbol{m}) = \mathrm{argmax}_m \left(\sum_{\varphi} (H(TOF(\varphi, \boldsymbol{m}), \varphi)) \right). \quad (1)$$

Weighting factors, initial guesses, priors, or constraints can also be seamlessly included in this type of maximization procedure. The overall workflow of the proposed method is summarized in Fig. 1(c). After obtaining the optimized parameters, the latter serve as an input to a single optimized reconstruction. Since only a single reconstruction step is required, this approach is much less computationally demanding as compared to alternative methods working in the image domain, which would generally require multiple reconstructions with trial and error parameter selection.

We tested the performance of our method in three numerical and experimental settings. Fig. 2 illustrates the results of our simulations done with the k-wave toolbox using a two-dimensional image domain of 472×472 pixels and 720 equally spaced projections covering 360° [8]. Fig. 2(a) depicts the energy absorption map of the original numerical phantom. SoS was set to $c_1 = 1700 m/s$ inside the

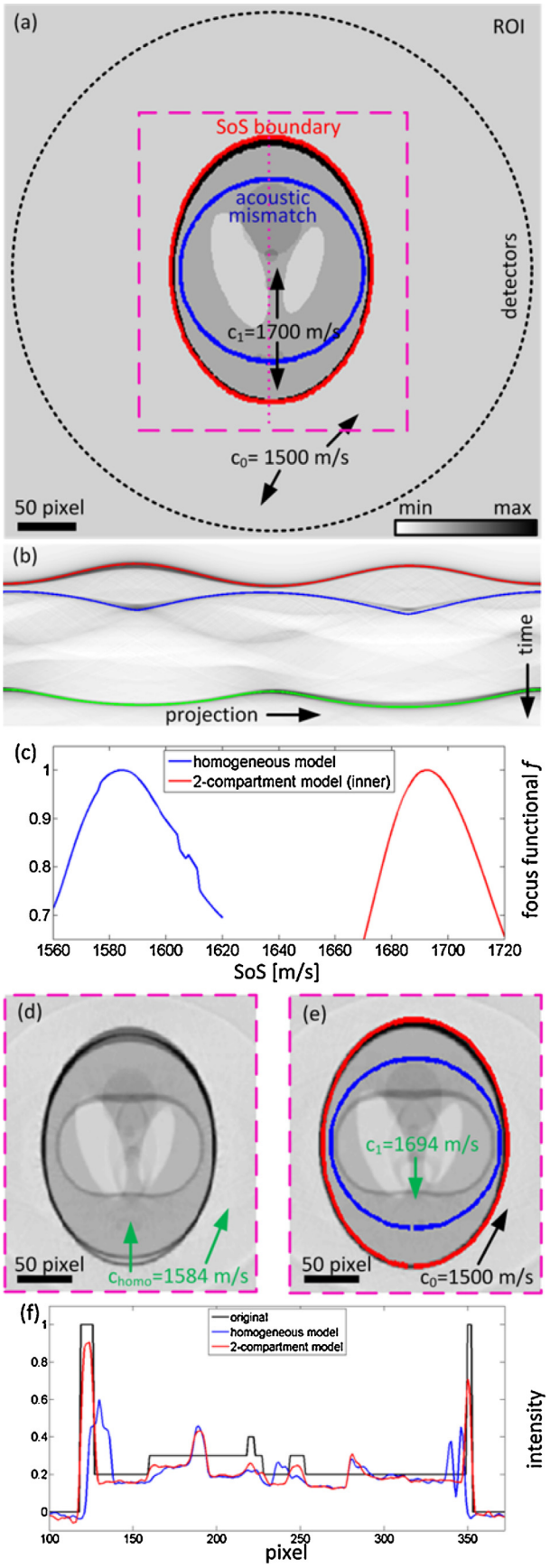

Fig. 2. Numerical simulation. (a) Original optical absorption distribution and acoustic properties: The SoS is $c_0 = 1500m/s$ outside of the red line and $c_1 = 1700m/s$ inside. An acoustic mismatch is indicated by the blue circle (twice the impedance inside). (b) Corresponding Hilbert-transformed sinogram with fitted signal characteristics corresponding to phantom boundary (red, *TOF1*), inner SoS (green, *TOF2*) and reflected signals (blue, *TOF3*). (c) Signal domain SoS focus function for homogeneous (blue) and proposed 2-compartmental model (red). (d) Optimized homogeneous reconstruction and (e) optimized 2-compartmental reconstruction of the central region (indicated by the dashed pink box in (a)) with parameters from signal domain analysis. The estimated shapes of the phantom and of the reflector are superimposed in red and blue, respectively. (f) Central vertical cross-section (dotted pink line in (a)) for original (black), optimized homogeneous (blue), and 2-compartmental model (red).

imaged object (enclosed by the red curve) and to $c_0 = 1500m/s$ outside. The blue circle having a radius of 80 pixels enclosed an acoustically mismatching area with twice the impedance of the surrounding medium. Fig. 2(b) presents the significant part of the corresponding Hilbert-transformed sinogram $H(t,\varphi)$. The subsequent detection of the rising edge on a per-projection basis resulted in a set of initial parameters for discerning the object's boundary. After maximization, the optimum $TOF1(\varphi, \boldsymbol{m})$ is plotted in Fig. 2(b) (red curve), representing the signals originating from the object's estimated boundary (approximately 1 pixel average deviation in the image domain from the original). Using the obtained compartment boundary as input for $TOF2(\varphi, \boldsymbol{m})$, a second maximization procedure initialized with $c_1 = 1500m/s$ yielded a SoS estimate for the inner compartment of $c_1 = 1694m/s$ (remaining error of 0.4%). The maximizing $TOF2(\varphi, \boldsymbol{m})$ is plotted in green in Fig. 2(b), representing the signals of the object's estimated boundary after transmission through the inner compartment. Next, by using the corresponding source locations on the compartment boundary and the determined SoS of the inner compartment, the optimization for $TOF3(\varphi, \boldsymbol{m})$ (blue curve, estimated reflected boundary signals) resulted in an estimated radius for the highly reflective boundary of 81.4 pixels, i.e. an error of 1.8% with respect to its original value. Fig. 2(c) plots the corresponding focusing function, which is the focusing functional value f as a function of the selected SoS within the object. It was calculated assuming either the 2-compartmental model (red curve) with $c_0 = 1500m/s$ outside of the object or the homogeneous (blue curve) SoS model with the respective maxima values at $c_{homo} = 1584m/s$ and $c_1 = 1694m/s$ corresponding to the optimal SoS selection.

Fig. 2(d) shows central region (dashed pink box in (a)) of the k-wave time reversal reconstruction using homogeneous propagation properties with $c_{homo} = 1584m/s$, no acoustic mismatch, and all other parameters as in the forward simulation. Fig. 2(e) shows the corresponding reconstruction using the SoS map obtained from signal domain analysis (i.e. object boundary, fixed SoS $c_0 = 1500m/s$ outside of the object, and estimated SoS $c_1 = 1694m/s$ within the object). The estimated object's boundary, SoS of the inner compartment, and location of the reflecting boundary are superimposed in red, green and blue, respectively. Finally, Fig. 2(f) plots the original and reconstructed image intensities along the phantom's central axis (dotted pink line in (a)) using the optimally selected SoS values. Clearly, the proposed 2-compartmental reconstruction approach deviated significantly less from the original values in the phantom in terms of absorbers' locations and magnitude. This is also reflected in an overall improved image root mean square deviation ($RMSD = \left(\sum_{n=pixels}\left(I_n - I_n^{orig}\right)^2 / \sum_{n=pixels}\left(I_n^{orig}\right)^2\right)^{0.5}$, where I is the reconstructed image and $I^{(orig)}$ is the original image) of $RMSD_{hetero} = 0.39$ as compared to $RMSD_{homo} = 0.95$ for the reconstruction assuming a homogenous SoS.

Experimental studies with an absorbing ink phantom were conducted for the purpose of further validation. For this, a commercial cross-sectional multi-spectral optoacoustic tomography (MSOT) small animal scanner (model: inVisionTF256, iThera Medical GmbH, Munich, Germany) was used. Technical details of the scanner are available elsewhere [15]. In short, for optoacoustic signal excitation it uses a pulsed optical parametric oscillator laser

tunable in the near-infrared spectral range from 670 nm up to 930 nm. The laser has 10 Hz pulse repetition rate and a maximum per-pulse energy of 100 mJ (model: SpitLight, InnoLas Laser GmbH, Krailling, Germany). Detection of signals originating from the imaged plane is subsequently done by a custom-made ultrasound array with 256 cylindrically-focused elements having a central frequency of 5 MHz, 70% relative bandwidth, and tomographic coverage of 266° around the imaged object (Imasonic SaS, Voray, France). The recorded optoacoustic responses were simultaneously digitized at the 256 projections with a sampling frequency of 40 MSa/s at 12 bit vertical resolution and transferred to a computer for live preview and further processing. The 15.9 mm diameter phantom used for validation consisted of solidified agar (1.8% w/w) mixed with a solution of India ink for attaining background absorption of approximately $\mu_a = 3.6cm^{-1}$ without addition of scattering substances like lipids (Fig. 3(a)). Several 200 μm diameter black polyethylene microspheres (Cospheric LLC, USA) were added to the phantom within the imaged plane. The data was acquired using 750 nm excitation wavelength. The measured optoacoustic signals were band-pass filtered between 100 kHz and 7 MHz to remove low frequency offsets and high frequency noise and the images were reconstructed iteratively using a MB reconstruction algorithm [6].

Fig. 3 illustrates the results from the ink phantom experiment. Fig. 3(b) shows the Hilbert-transformed sinogram $H(t,\varphi)$ of the measured data having characteristic signal features originating from the phantom boundary and the microspheres. The estimated boundary resulting from the $TOF1(\varphi,\boldsymbol{m})$ fitting is depicted by the red line, assuming a SoS in water of $c_0 = 1517m/s$ at the measured water temperature of 34 °C. Note that signals were only available from a partial angle covering less than 360°. The optimization yielded an average object diameter of 15.8 mm, i.e. 0.5% smaller than the actual inner diameter of the syringe (3/8 inch) used to mold the phantom. The subsequent $TOF2(\varphi,\boldsymbol{m})$ optimization resulted in a SoS of $c_1 = 1537m/s$ within the object (green line). In contrast, one obtained a SoS of $c_{homo} = 1523m/s$ when optimizing the functional f for the homogenous SoS case (solid blue curve in Fig. 3(c)). A similar, post-reconstruction search for the optimal SoS in the image domain using a Tenenbaum gradient [8] focus measure (dashed blue curve) yielded a very similar value, thus validating the optimal SoS choice obtained via the signal domain analysis. Fig. 3(d) shows the reconstructed image when using the optimized homogeneous SoS while Fig. 3(e) shows the reconstructed image when using optimized heterogeneous parameters with the estimated phantom outline superimposed in red. All the microspheres were resolved via optimization of both homogeneous and heterogeneous models with no substantial differences in the image quality observed. In this particular case, the use of a heterogeneous SoS model was not crucial owing to the relatively small SoS difference between imaged object and surrounding water.

Finally, Fig. 4 presents the results obtained with the dataset acquired from the first author's index finger. The finger was imaged in the area between peripheral and distal interphalangeal joints using the same MSOT scanner [13]. The dorsal side of the finger was facing the detection array while the imaging was done at either 690 nm or 900 nm excitation wavelength. At 690 nm, melanin exhibits the highest contribution to the image contrast whereas at 900 nm the vasculature with main contributions from oxygenated hemoglobin is dominant (Fig. 4(a)). Fig. 4(b) shows the MB reconstruction at 900 nm excitation assuming a homogeneous SoS of 1542 m/s, a value that was obtained by optimization in the post-reconstruction image domain. At this excitation wavelength, the vasculature stands out as the most dominant feature in the images whereas effects of smearing and reflections by the bone can be clearly recognized (green circles and blue arrows). Furthermore, the skin surface can be readily identified while the incomplete tomographic angular coverage has resulted in additional artifacts visible at the bottom (palmar) part of the image.

The Hilbert-transformed sinogram of the finger's cross-section acquired at 690 nm is shown in Fig. 4(c). This data was chosen for the signal domain analysis because of the dominating melanin absorption at the lower wavelengths and thus stronger signals generated from the skin. The fits for the skin surface ($TOF1(\varphi,\boldsymbol{m})$, shown by the red curve), inner SoS ($c_1 = 1610m/s$, green curve), and skin reflection at the bone surface (blue curve) have been

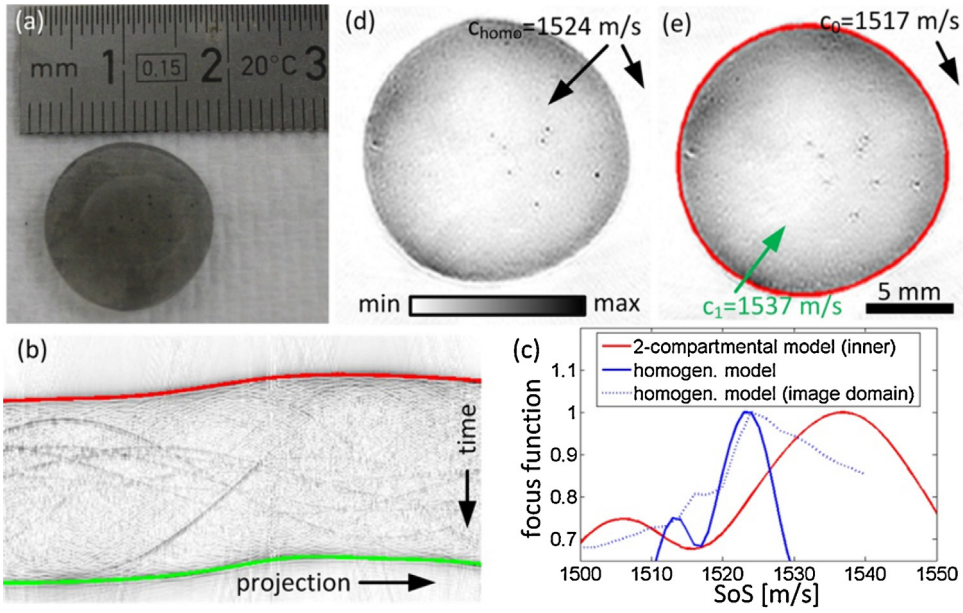

Fig. 3. Experimental ink phantom study. (a) Photograph of the central slice of the highly absorbing ink phantom with several microspheres (cut after imaging). (b) Hilbert-transformed measured signals with *TOF1* (red) and *TOF2* fits (green) to determine object shape and SoS within the object, respectively, superimposed. (c) SoS focus function for a 2-compartmental model obtained in the signal domain via *TOF2* (red), corresponding signal domain focus function assuming a homogenous SoS (solid blue), and homogeneous image domain Tenenbaum gradient focus function (dashed blue). The respective maxima are $c_1 = 1537m/s$, $c_{homo} = 1523m/s$, and $c_{homo} = 1524m/s$.(d) Optimized homogeneous and (e) optimized heterogeneous reconstruction of the phantom with the estimated object shape superimposed in red.

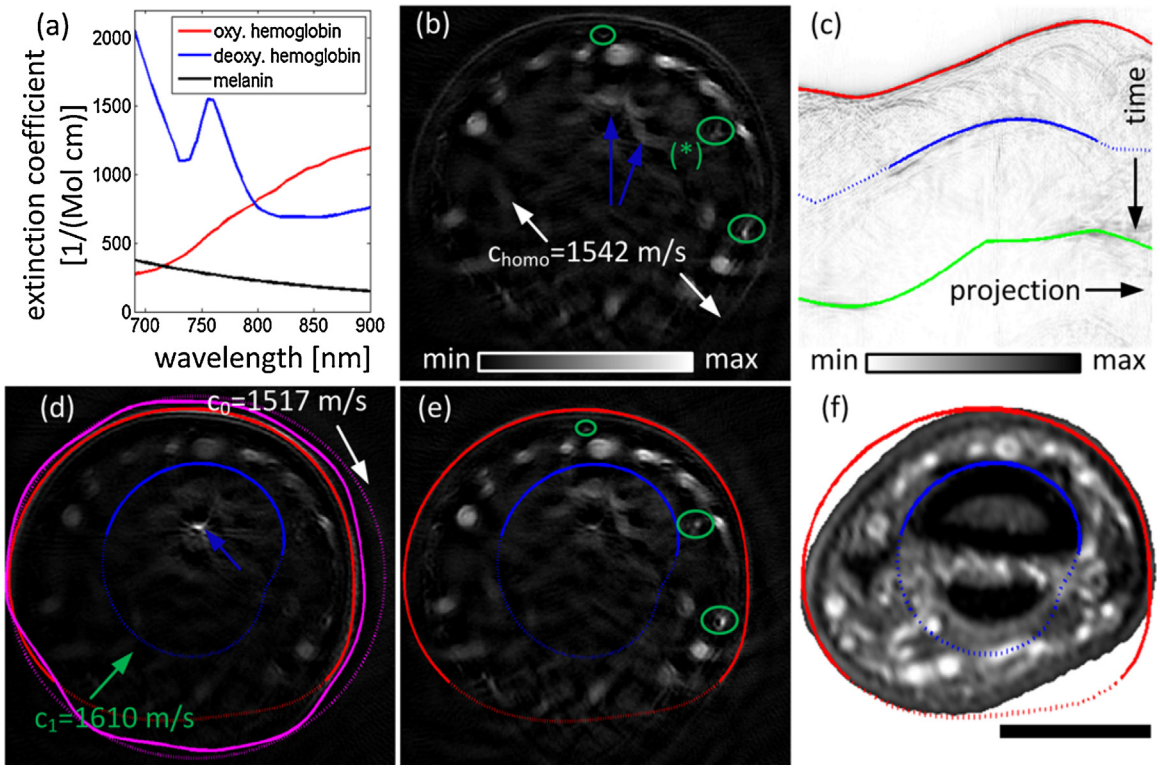

Fig. 4. Results attained from in vivo human finger data. (a) Absorption spectra of the three main chromophores in the near-infrared. At higher wavelengths, the relative absorption of blood is the highest with main contribution stemming from the oxygenated hemoglobin. For lower wavelengths, significant contributions stem from melanin as well. (b) Cross-sectional reconstruction of a finger at 900 nm excitation wavelength with best homogeneous SoS ($c_{homo} = 1542 m/s$). Blue arrows represent reflection artifacts induced by the bone. (c) Hilbert-transformed sinogram at 690 nm excitation with fits for finger shape (red), inner SoS (green) and bone (blue). (d) Corresponding reconstruction using optimized 2-compartmental model parameters ($c_1 = 1610 m/s$ within the red curve) obtained from signal domain analysis. The pink line indicates the final segmentation (solid) obtained from an active contour image domain segmentation based on a manually selected initial guess (dotted). (e) Same reconstruction for 900 nm excitation wavelength with improved image quality over the homogeneous model (green circles). (f) Slice of the finger acquired using MRI with the superimposed location of the skin (red) and bone (blue) as estimated by MSOT. Manual registration was done based on the dorsal vascular of the MRI slice and of the MSOT reconstruction in (e). Scale bar corresponds to 1 cm.

superimposed onto the sinogram. Fig. 4(d) presents the corresponding reconstruction using the optimized model parameters. The estimated shape of the finger (red) agreed well with the actually reconstructed skin outline. On the other hand, the estimated shape of the bone (blue) did not correlate with any absorbing structures in the reconstructed image. This is not surprising since the bone is only weakly absorbing compared to blood, thus mainly affecting the images by generating acoustic reflections at its surface. Note that the solid lines in Fig. 4(d) indicate boundary segments which were directly extracted from the measured signals while the dashed segments are based on extrapolations for the remaining angles and might therefore not necessarily coincide with real structures.

In order to compare the performance of our signal domain segmentation algorithm with an image domain segmentation approach, we performed an active contour segmentation of the images using the active contour toolbox without manually optimizing the default parameters [16]. Starting with a manually selected initial guess (dotted pink ellipse) has rendered the final segmentation as shown by the solid pink line. The obtained image domain segmentation indicates that the proposed signal domain analysis yielded results of at least similar or even better quality. Indeed, advanced image segmentation methods may produce more accurate results, yet would commonly require additional computational complexity and dedicated optimized settings.

Applying the optimized SoS map has similarly resulted in improvements for the image acquired at 900 nm (Fig. 4(e)), in which the small vessels (labeled with green circles) appeared with a better shape and contrast as compared to Fig. 4(b) that was obtained after image domain focusing and using a homogeneous SoS model. To better quantify the improved focusing performance, a 2-D Gaussian was fitted to the vessel indicated by the green asterisk in Fig. 4(b) for reconstructions obtained using both homogeneous and heterogeneous models (Fig. 4(b) and (f)). Besides an increased magnitude (maximum intensity value of 1.1 (a.u.) compared to 0.79 (a.u.)), the heterogenous model resulted in a similar focal FWHM of 864 μm in the vertical direction (compared to 875 μm in the homogenous case) and a 22% improved FWHM of 301 μm in the horizontal direction (compared to 387 μm in the homogeneous case).

To further validate the attained betterments, the same finger was imaged using a 3 T MRI system (Verio, Siemens AG, Erlangen, Germany) and a flexible surface coil (flex large, Siemens AG, Erlangen, Germany). Fig. 4(f) shows the MRI cross-section acquired approximately from the same location as for the MSOT images. Manual registration of the images was then done by using dorsal vasculature as reference points with the estimated shapes of the skin and bone indicated by the red and the blue curve, respectively. Apparently, soft tissue deformations and a different finger position during the MRI acquisition have led to deviations in the lower (palmar) part of the image, but all major vessels in the MRI image had a matching one in the MSOT (Fig. 4(e)). In the upper part of the image, the estimated skin surface agreed well with the MRI image, whereas the quality of the fits was lower in the lower part of the image, mainly due to the lack of tomographic information from the limited-view detection in the MSOT scanner and soft tissue

deformations. Likewise, the estimated location of the bone agreed well with the MRI for the dorsal side while the extrapolated segments showed large deviations, again due to the missing optoacoustic tomographic data from the corresponding angles.

The angular dependence of $H(t,\varphi)$ can be interpreted as follows. The optoacoustic signals transmitted through the finger were mainly detected at the radial and ulnar (lateral) sides of the finger because the bone did almost not influence these signal propagation paths. The central detectors (located in front of the dorsal part of the finger) did not measure transmitted signals from the palmar side as the bone reflected most of those signals. The ulnar and radial bone delineation was further complicated due to the higher curvature of the bone surface in these areas and the geometrical alignment of skin, bone, and detectors. Delineation of the palmar part of the bone completely failed due to the limited-view setup and lack of tomographic information while the extrapolated outline did not render the true shape of the bone.

The proposed signal domain analysis approach comes with three major advantages over the alternative optimization methods operating in the image domain. First, its segmentation and SoS optimization performance is not affected by image domain artifacts, such as streak and other artifacts related to the limited-view tomographic geometry [17]. Second, it is computationally efficient because only one single reconstruction cycle is needed as compared to multiple cycles required by the image domain optimization algorithms [11]. This is of special importance when employing the MB reconstruction framework to account for a heterogeneous SoS distribution in the medium, which is often associated with a significantly higher computational load as compared to its counterpart assuming an acoustically homogenous medium [6]. Third, delineation of some strongly reflecting structures, such as bones, cannot be reliably performed in the image domain if these structures are not optically absorbing and produce no optoacoustic contrast, but only reflection artifacts.

Further refinements of the method are possible by operating on full tomographic datasets having 360° coverage around the object [14], incorporating multispectral processing, or exploiting additional frequency domain features of the detected signals via cross-correlation or wavelet-based methods. Another future direction will evaluate the possibility of including three (or more) compartments into the model, thus potentially further enhancing the image quality by modeling of the scattered signals. The proposed signal domain segmentation is readily applicable to many other imaging geometries, e.g. handheld scanners or raster-scanning systems [18,19], that often provide only a reduced detection surface aperture. Also in imaging with such systems, the skin surface is typically smooth and flat while single vessels could provide dominant features to be used as the guide stars for SoS estimation in the tissue (instead of SoS estimation from transmission for >180° coverage). In addition, similar methodology can be implemented in 3-D tomography geometries using 2-D boundary parameterizations. Besides improving the image quality, the signal domain segmentation possibly allows for simple detection of motion due to e.g. breathing, which can be subsequently used for efficient retrospective gating or clustering. On the other hand, applicability of the method is limited when imaging irregularly shaped objects or in cases where distribution of the acoustic and optical properties in the object is highly uncorrelated.

In summary, a signal domain segmentation algorithm was developed that exploits characteristic signal features in order to perform object segmentation and retrieve optimal acoustic reconstruction parameters prior to image reconstruction, which results in improved image quality and considerable computational gains versus alternative methods performing the segmentation and parameter optimization in the image domain. The suggested technique was successfully evaluated in numerical simulations, experimental phantom measurements, and cross-sectional image data acquired from a human finger. The proposed signal domain segmentation thus offers a robust methodology for image quality enhancement in tomographic optoacoustic imaging.

Conflict of interest

None.

Acknowledgements

D.R. acknowledges funding from the European Union under grant agreement *ERC-2010-StG-260991*.

R.M. acknowledges funding from the German Research Foundation (DFG) under grant agreement *DFG-ME3718/2-1*.

References

[1] V. Ntziachristos, D. Razansky, Molecular imaging by means of multispectral optoacoustic tomography (MSOT), Chem Rev 110 (2010) 2783–2794.
[2] B. Cox, J.G. Laufer, S.R. Arridge, P.C. Beard, Quantitative spectroscopic photoacoustic imaging: a review, Journal of Biomedical Optics 17 (2012).
[3] P. Beard, Biomedical photoacoustic imaging, Interface Focus 1 (2011) 602–631.
[4] C. Lutzweiler, D. Razansky, Optoacoustic imaging and tomography: reconstruction approaches and outstanding challenges in image performance and quantification, Sensors 13 (2013) 7345–7384.
[5] C. Yoon, J. Kang, S. Han, Y. Yoo, T.-K. Song, J.H. Chang, Enhancement of photoacoustic image quality by sound speed correction: ex vivo evaluation, Optics express 20 (2012) 3082–3090.
[6] X.L. Dean-Ben, V. Ntziachristos, D. Razansky, Acceleration of optoacoustic model-based reconstruction using angular image discretization, Medical Imaging, IEEE Transactions on 31 (2012) 1154–1162.
[7] D. Modgil, M.A. Anastasio, P.J. La Riviere, Image reconstruction in photoacoustic tomography with variable speed of sound using a higher-order geometrical acoustics approximation, Journal of Biomedical Optics 15 (2010).
[8] B.E. Treeby, B.T. Cox, k-Wave: MATLAB toolbox for the simulation and reconstruction of photoacoustic wave fields, Journal of biomedical optics 15 (2010), pp. 021314-021314-12.
[9] C. Huang, K. Wang, L. Nie, L.V. Wang, M.A. Anastasio, Full-wave iterative image reconstruction in photoacoustic tomography with acoustically inhomogeneous media, Medical Imaging, IEEE Transactions on 32 (2013) 1097–1110.
[10] J. Jose, R.G.H. Willemink, S. Resink, D. Piras, J.C.G. van Hespen, C.H. Slump, W. Steenbergen, T.G. van Leeuwen, S. Manohar, Passive element enriched photoacoustic computed tomography (PER PACT) for simultaneous imaging of acoustic propagation properties and light absorption, Optics Express 19 (2011) 2093–2104.
[11] S. Mandal, E. Nasonova, X.L. Deán-Ben, D. Razansky, Optimal self-calibration of tomographic reconstruction parameters in whole-body small animal optoacoustic imaging, Photoacoustics 2 (2014) 128–136.
[12] M.A. Anastasio, J. Zhang, X.C. Pan, Y. Zou, G. Ku, L.H.V. Wang, Half-time image reconstruction in thermoacoustic tomography, Ieee Transactions on Medical Imaging 24 (2005) 199–210.
[13] C. Lutzweiler, R. Meier, E. Rummeny, V. Ntziachristos, D. Razansky, Real-time optoacoustic tomography of indocyanine green perfusion and oxygenation parameters in human finger vasculature, Optics letters 39 (2014) 4061–4064.
[14] P. van Es, S. Biswas, H. Moens, W. Steenbergen, S. Manohar, Initial results of finger imaging using photoacoustic computed tomography, Journal of biomedical optics 19 (2014) 60501.
[15] A. Dima, N.C. Burton, V. Ntziachristos, Multispectral optoacoustic tomography at 64, 128, and 256 channels, Journal of biomedical optics 19 (2014), pp. 036021-036021.
[16] E. Debreuve, "Active Contour Toolbox", Matlab Central File Exchange, 2006 05 Jul accessed 22 Oct 2015 (http://www.mathworks.com/matlabcentral/fileexchange/11643-active-contour-toolbox).
[17] J. Frikel, E.T. Quinto, Characterization and reduction of artifacts in limited angle tomography, Inverse Problems 29 (2013) 125007.
[18] A. Buehler, M. Kacprowicz, A. Taruttis, V. Ntziachristos, Real-time handheld multispectral optoacoustic imaging, Optics letters 38 (2013) 1404–1406.
[19] R. Ma, S. Söntges, S. Shoham, V. Ntziachristos, D. Razansky, Fast scanning coaxial optoacoustic microscopy, Biomedical optics express 3 (2012) 1724–1731.

Christian Lutzweiler is currently pursuing a PhD in biomedical engineering at Chair of Biological Imaging, TU München, and at Institute for Biological and Medical Imaging, Helmholtz Zentrum München. He received his diploma of physics from Karlsruhe Institute of Technology. His main research interests include

reconstruction problems in photoacoustic imaging and clinical imaging studies using multispectral optoacoustic tomography.

Reinhard Meier, MD, is Professor of Radiology and Vice-Chairman of the Department of Diagnostic and Interventional Radiology at the University Hospital of Ulm. Furthermore, he is director of the Lab 'Translational Molecular Imaging' at the Department of Diagnostic and Interventional Radiology, Technical University Munich. He completed his postdoctoral training at the University of California San Francisco. The purpose of his research is to translate molecular imaging technologies from bench to bedside. As an example, he introduced optical imaging for detection and therapy monitoring of rheumatoid arthritis in the hand of patients to his clinic.

Daniel Razansky is the Professor of Molecular Imaging Engineering at the Technical University of Munich and the Institute for Biological and Medical Imaging, Helmholtz Center Munich. He earned his degrees in Electrical and Biomedical Engineering from the Technion – Israel Institute of Technology and completed a postdoctoral training at the Harvard Medical School. His Lab works at the interface of engineering, biology and medicine to devise novel tools for high performance functional and molecular imaging. In particular, new imaging paradigms based on biomedical optics, optoacoustics, ultrasound and their synergistic combinations are developed to enable multi-scale observations with unprecedented spatiotemporal resolution and penetration of several millimeters to centimeters into living intact organisms.